Seeded growth synthesis of Au-Fe$_3$O$_4$ heterostructured nanocrystals: rational design and mechanistic insights

Elvira Fantechi,[a] Alejandro G. Roca,[a*] Borja Sèpulveda,[a] Pau Torruella,[b] Sonia Estradé,[b] Francesca Peiró,[b] Emerson Coy,[c] Stefan Jurga,[cd] Neus G. Bastús,[a] Josep Nogués,[ae] Víctor Puntes[aef*]*

[a] Catalan Institute of Nanoscience and Nanotechnology (ICN2), CSIC and The Barcelona Institute of Science and Technology (BIST), Campus UAB, Bellaterra, 08193 Barcelona, Spain.

[b] Laboratory of Electron Nanoscopies (LENS) – MIND-IN2UB, Department d'Electronica, Universitat de Barcelona, carrer Martí i Franquès 1, 08028, Barcelona, Spain

[c] NanoBioMedical Centre, Adam Mickiewicz University, Umultowska 85, 61-614 Poznań, Poland

[d] Faculty of Physics, Adam Mickiewicz University, Umultowska 85, 61-614 Poznań, Poland

[e] ICREA, passeig Llus Companys 23, 08010 Barcelona, Spain

[f] Vall d'Hebron Institut de Recerca (VHIR), 08035, Barcelona, Spain.

*e.fantechi@gmail.com *alejandrogroca@gmail.com *victor.puntes@icn.cat

ABSTRACT: Multifunctional hybrid nanoparticles comprising two or more entities with different functional properties are gaining ample significance in industry and research. Due to its combination of properties, a particularly appealing example is Au-Fe$_3$O$_4$ composite nanoparticles. Here we present an in-depth study of the synthesis of Au-Fe$_3$O$_4$ heterostructured nanocrystals (HNCs) by thermal decomposition of iron precursors in the presence of preformed 10 nm Au seeds. The role of diverse reaction parameters on the HNCs formation was investigated using two different precursors: iron pentacarbonyl (Fe(CO)$_5$) and iron acetylacetonate (Fe(acac)$_3$). The reaction conditions promoting the heterogeneous nucleation of Fe$_3$O$_4$ onto Au seeds were found to significantly differ depending on the precursor chosen, where Fe(acac)$_3$ is considerably more sensitive to the variation of the parameters than Fe(CO)$_5$, and more subject to homogenous nucleation processes with the consequent formation of isolated iron oxide nanocrystals (NCs). The role of the surfactants was also crucial in the formation of well-defined and monodisperse HNCs by regulating the access to the Au surface. Similarly, the variation of the [Fe]:[Au] ratio, temperature and employed solvent were found to act on the mean size and on the morphology of the obtained products. Importantly, while the optical properties are rather sensitive to the final morphology, the magnetic ones are rather similar for the different types of obtained HNCs. The surface functionalization of dimer-like HNCs with silica allows their dispersion in aqueous media, opening the path to their use in biomedical applications.

Introduction

In recent years, nanochemistry research has moved towards the realization of complex multifunctional heterostructured nanocrystals (HNCs), able to combine two or more different inorganic materials in a single nanosystem by a direct atomic bond at their interphase without the presence of any molecular bridge. These heterostructured systems provide new degrees of freedom to control nanocrystals (NCs) functionality.[1–6] In this context, the combination of gold (Au) and magnetite (Fe_3O_4) into one nanostructure has attracted a great interest due to the enormous potential of this type of structure in a wide range of applications such as catalysis,[7–11] optics,[12,13] electronics,[14] sensing,[9,15] and biomedicine.[9] Indeed, the integration of both magnetic and plasmonic properties in a single nanosystem makes Au-Fe_3O_4 HNCs extremely promising for the improvement of the related applications and the development of new ones.[9] For example, the two functionalities can act in a synergic way, enhancing specific properties (e.g., heat release capability, catalytic activity) or serving as contrast agents allowing combination of the high spatial resolution of computed axial tomography (CAT) imaging with the high sensitivity of magnetic resonance imaging (MRI). Moreover, the study of the Au-Fe_3O_4 interphase and the interaction between the magnetic and plasmonic domains as a function of the morphology make these systems very interesting also from a fundamental point of view.

Au-Fe_3O_4 HNCs with a precise control over their size and morphology can be obtained by thermal decomposition, following a seeded-growth approach in which the iron oxide counterpart grows onto the gold NC surface. Although the Au seeds can be obtained in a previous step or *in situ*, the first approach usually offers a better control on the monodispersity of the obtained HNCs with respect to the one-pot reaction. The most common iron oxide precursors used for this synthesis have been iron pentacarbonyl ($Fe(CO)_5$),[16,17] iron(III)acetylacetonate ($Fe(acac)_3$)[18] and

iron(III) oleate,[19–21] where the [Fe]:[Au] molar ratio, together with surfactants, solvent, heating rate and reaction time were employed to control the morphology.

Despite the great interest raised by Au-Fe₃O₄ HNCs, the mechanism of formation and role of the diverse synthetic parameters to achieve different morphologies are still not fully understood and are, in fact, not free of controversy.[16,17] Additionally, no comparison has been reported yet between the structural and physical properties of Au-Fe₃O₄ HNCs obtained from different iron precursors, since it is known the iron oxide moiety can be strongly influenced by the kind of precursor used, where, for example, some precursors and processes can give secondary uncontrolled iron phases (e.g., Fe or Fe₁₋ₓO).[22–27]

The purpose of this work is to investigate the effect of the different reaction parameters on the morphology of Au-Fe₃O₄ HNCs obtained by thermal decomposition of iron precursors (Fe(CO)₅ and Fe(acac)₃) in the presence of preformed Au NCs. In particular, the aim is to define the optimal conditions for the formation of dimers and flower-like HNCs, which are of particularly interest compared to the core-shell morphology, since these morphologies have both domains exposed. It must be noted that the heterogeneous nucleation of iron oxide onto gold surfaces is not a trivial process, because of the large lattice mismatch (~3%) between the two phases. Within this context, the seeded-growth strategy was systematically investigated by changing the iron oxide precursor (Fe(CO)₅ or Fe(acac)₃), Fe precursor/Au seed ratio, surfactant/Fe ratio and concentration, solvent and temperature. Fe(CO)₅ has been largely reported as precursor in the formation of Au-Fe₃O₄ HNCs, however its use presents some issues related to toxicity, stability and high cost,[28] factors that can hamper a scale-up procedure. In contrast, Fe(acac)₃ has several advantages related to its stability, low cost and low toxicity.[29,30] Besides, despite Fe(acac)₃ has been widely used as iron precursor for the synthesis of pure iron oxide NCs, its use in the

formation of Au-Fe$_3$O$_4$ HNCs is rather uncommon.[18,31] The characterization of the obtained products highlights that the conditions required for the controlled formation of Au-Fe$_3$O$_4$ HNCs and their morphology critically depend on the iron precursor chosen, as much as on the surfactants, temperature, time and the other reaction conditions. Finally, considering the great interest of these heterostructures for their use as multifunctional nanoplatforms in biomedical applications, silica coating was demonstrated to be a feasible and effective strategy to transfer Au-Fe$_3$O$_4$ HNCs from organic to aqueous media.

Experimental section.

The detailed synthetic procedures for all the samples presented in this article can be found in the Supporting Information (SI).

Materials

All the samples were prepared under Ar atmosphere using commercially available reagents. Hexane ($\geq$95%), phenyl ether (Ph$_2$O) (99%), benzyl ether (Bz$_2$O) ($\geq$98%), 1-octadecene (ODE) (90%), oleic acid (Ol-COOH) (90%), gold(III) chloride trihydrate ($\geq$ 99.9%), iron(III) acetylacetonate ($\geq$99.9 %), iron(0) pentacarbonyl ($\geq$99.99%), IGEPAL® CO-520 (average Mn 441), Tetraethyl orthosilicate (TEOS, $\geq$99.0%) were purchased from Aldrich Chemical Co. and 1,2-dodecanediol (DDD) ($\geq$90%) from Fluka. Oleylamine (Ol-NH$_2$) (80-90%) was purchased from Acros Organics. Ethanol (96%) was from PanReac AppliChem, while 2- propanol (99%) and methanol (98.5%) were from VWR Chemicals. Ammonia solution (28-30%) was from Merk. All chemicals were used as received.

Synthesis of Au-Fe$_3$O$_4$ HNCs from Fe(CO)$_5$ (HNCs_CO).

A mixture of Au NCs (0.035 g in ~6 mL of hexane, from sample **Au NCs_A**; see SI for details on the synthesis of the Au NCs

seeds), oleylamine (0.247 g, 0.92 mmol), oleic acid (0.261 g, 0.92 mmol) and 1-octadecene (20 mL) was heated up to 120 °C under vacuum in order to remove the hexane and the residual moisture. Later, $Fe(CO)_5$ (0.05 mL, 0.37 mmol) was injected into the reaction and the temperature was increased to 315 ºC at 4 ºC/min under argon flow. Finally, the reaction was kept at 315 ºC for 50 min. The mixture was removed from the heating source and allowed to cool down to room temperature before exposing it to air. The HNCs suspension was purified by centrifuging twice the reaction mixture with a mixture of 2-propanol and methanol and further redispersion in hexane.

Synthesis of Au-Fe₃O₄ HNCs from Fe(acac)₃ (HNCs_acac). A mixture of Au NCs (0.011 g in ~3 mL of hexane, from sample **Au NCs_B**; see SI), $Fe(acac)_3$ (0.177 g, 0.5 mmol), 1,2-dodecanediol (0.508g, 2.5 mmol), oleylamine (0.53 g, 2 mmol), oleic acid (0.565 g, 2 mmol) and 1-octadecene (50 mL) was heated up to 205 °C at 5 °C/min under Ar flow (under vacuum until 115 ºC in order to remove the hexane and the residual moisture) and kept at this temperature for 2 h. Then, the reaction was heated up to 315 °C at 6 ºC/min and kept at this temperature for 2 h before removing it from the heating source and allowed to cool down to room temperature before exposit it to air. The HNCs suspensions were purified by first centrifuging twice the reaction moisture with a mixture of 2-propanol and methanol and further redispersion in hexane.

Silica coating of Au-Fe₃O₄ HNCs. Silica coating was performed using a reverse-micelles method. Briefly, 0.35 mL of IGEPAL® CO-520 were added to a 6 mL of suspension Au-Fe₃O₄ HNCs in cyclohexane ($1.5 \cdot 10^{13}$ HNCs/mL) and gently stirred mechanically, resulting in a clear solution. Then, 200 µL of an ammonia solution (28-30%) and 20 µL of tetraethyl orthosilicate (TEOS) were added, shaking the suspension between both additions. The resulting mixture was kept at room temperature for 24 h and then 5 mL of methanol were added to stop the reaction.

The obtained Au-Fe$_3$O$_4$ HNCs@SiO$_2$ were recovered by centrifugation of the polar phase and dispersed in a mixture of water and methanol with a 1:1 ratio.

Characterization.

Morphology, particle size and size distribution of the samples were determined by transmission electron microscopy (TEM), using a 120 kV JEOL JEM-1400 microscope. High resolution-TEM images, Scanning-TEM (STEM) High Angle Annular Dark Field (HAADF) images, Electron Energy Loss Spectroscopy (EELS) measurements were performed in a JEOL ARM200f TEM equipped with a JEOL EDX detector, a Gatan Quantum GIF EELS spectrometer and a Field Emission Gun operated at 200kV. Analysis of the TEM images was performed with Gatan Digital Micrograph software. The samples were prepared by drop-drying a diluted hexane suspension of the samples onto 200 mesh holey carbon-coated copper grids. The mean diameter and the size distribution of each sample were obtained by statistical analysis over 200-600 particles, analyzing the recorded images with the ImageJ software.[32] For non-spherical shaped objects, the size measurements were performed as schematized in **Figure S1**.

Powder X-ray diffraction measurements were performed with a PANalytical X'PERT PRO MPD X-ray Diffractometer using CuK$_\alpha$ radiation and operating in θ–2θ Bragg Brentano geometry at 40 kV and 40 mA. The lattice parameters of each single phase were evaluated using the software MAUD.[33] The determination of the mean crystallite diameter, d$_{XRD}$, was performed on the (111) and (311) peaks for Au and magnetite phase, respectively, using the Debye-Scherrer's equation.

UV-VIS spectra were recorded using a Shimadzu UV-2100 spectrometer in the 300-800 nm range using 5 mL quartz cuvettes.

Magnetic measurements were performed a MPMSXL-7 Quantum Design SQUID magnetometer. Samples were tightly packed onto a Teflon tape in order to prevent preferential orientation. Zero Field Cooled-Field Cooled (ZFC/FC) curves were obtained by measuring the magnetization as a function of temperature, after cooling the sample in the presence (FC) or in the absence (ZFC) of an applied magnetic field (2.5 mT).

Results and Discussion

Conventionally, the process of formation of NCs is composed by two different steps: the formation of small nuclei (homogenous nucleation) and their successive growth, leading to the final NCs.[34,35] When applied to the synthesis of Au-Fe_3O_4 HNCs through the seeded-growth approach, the nucleation step assumes a crucial role in obtaining HNCs and in determining their final morphology. In **Figure 1** are summarized the possible different pathways occurring when an iron precursor is decomposed in a hot solution containing Au NCs. Au-Fe_3O_4 HNCs are obtained when the process of heterogeneous nucleation of iron oxide onto the Au NCs surface (**Figure 1a**) is favored with respect to homogenous nucleation (**Figure 1b**), which would lead to the formation of isolated iron oxide NCs. Once the optimal conditions for heterogeneous nucleation are ensured, it is then possible to investigate the different reaction parameters involved in the formation of different HNCs morphologies and in the growth of the formed iron oxide domains.
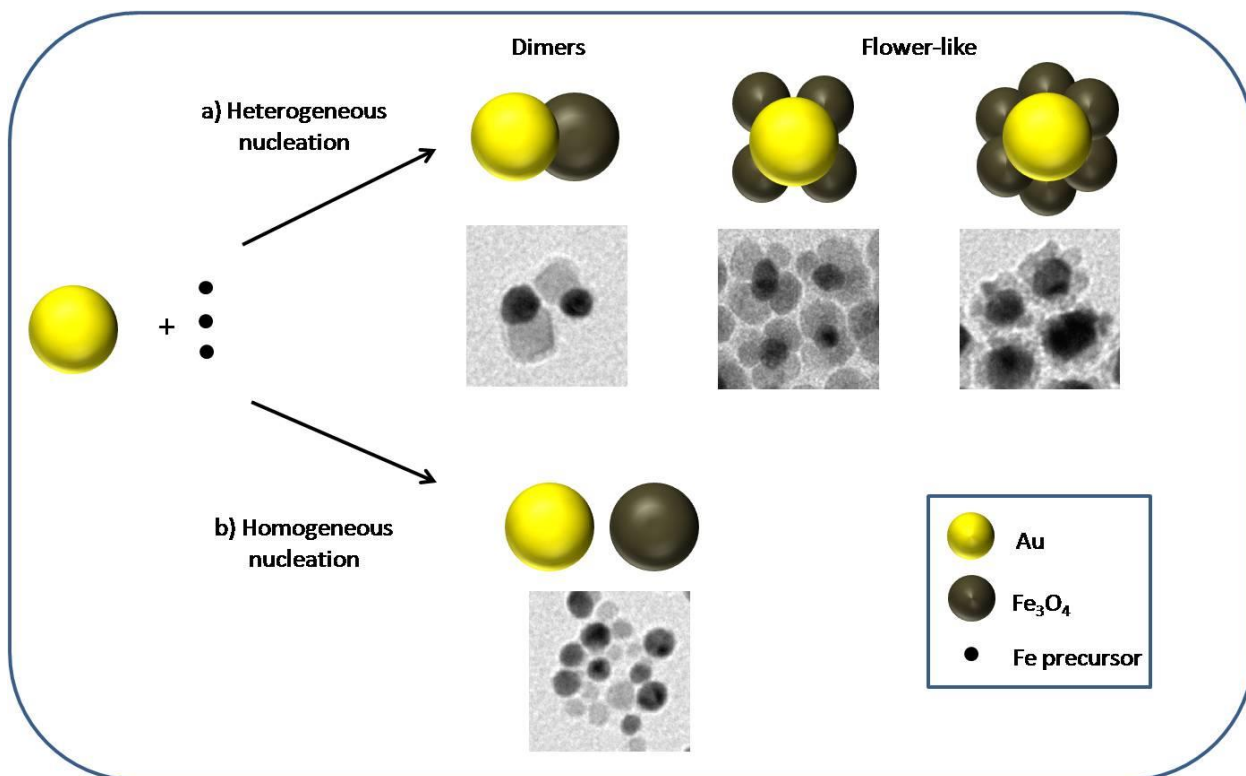
Figure 1: Schematic representation of the possible pathways of the seeded-growth reaction, starting from a mixture of Au NCs and molecules of iron precursor. a) Heterogeneous nucleation of iron oxide, with the formation of either dimers or flower-like HNCs; b) Homogeneous nucleation of iron oxide, with the consequent formation of isolated iron oxide NCs.

Monodisperse Au-Fe$_3$O$_4$ HNCs with dimer morphology (**HNCs_CO**, **Figure 2a**) were obtained by decomposition of Fe(CO)$_5$ on preformed oleylamine capped Au NCs (sample **Au NCs_A**) in 1-octadecene (ODE), following a modified procedure from Grzybowski *et al.*.[17] The obtained HNCs show a total length around 22 nm, with a mean size of the iron oxide domain (see **Figure S1**) of around 10 nm. Note that when the Au and Fe$_3$O$_4$ counterparts do not form heterostructures, as in the case of a mixture of independent Au and Fe$_3$O$_4$ nanocrystals (**Figure S4**), they tend to cluster in Au and Fe$_3$O$_4$ rich areas, and the formed nanoparticles are clearly separate from each other by several nm due to thickness of their respective surfactant coating layers. As expected, no significant change, due to reactive etching, was observed in the mean size of the Au domains if compared to those of the starting Au NCs used as seeds (**Figure S5**).

9

Importantly, for almost each of the Au domains (~96%) corresponds a single iron oxide counterpart and no presence of isolated Fe_3O_4 or a secondary population with multiple iron oxide domains was detected. The minority population of unreacted isolated Au NCs can be easily purified through magnetic separation. Starting from these reaction conditions and taking sample **HNCs_CO** as a reference, the effect of the different synthetic conditions was investigated in order to individuate the key parameters involved in the control of the nucleation of iron oxide on top of Au NCs and its successive growth.
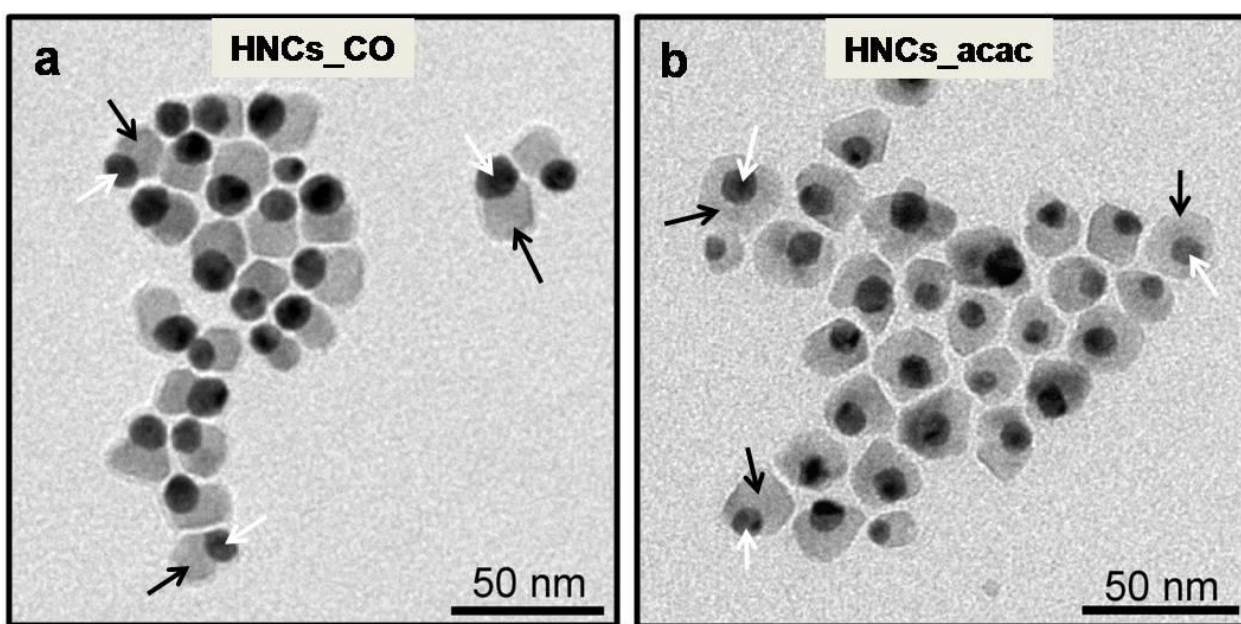

Figure 2: Representative TEM pictures of Au-Fe_3O_4 HNCs obtained a) from $Fe(CO)_5$ (**HNCs_CO**) and b) form $Fe(acac)_3$ (**HNCs_acac**) precursors. The light and dark arrows identify the Au and iron oxide domains, respectively. Note that in our bright field TEM images, darker contrast corresponds to gold, while lighter contrast to iron oxide as a consequence of their difference in electron density.

Effect of the iron precursor. In the first instance, the effects of the nature of the iron oxide precursors were evaluated. Remarkably, when $Fe(acac)_3$ was used instead of $Fe(CO)_5$, keeping constant all the other reaction parameters, significant differences were observed in the morphology of the formed HNCs. As it can be observed (**Figure 3a**), the Au NCs are surrounded by more than one iron oxide domain, with less than 20% of binary dimer HNCs and they show a

more rounded shape instead of the elongated one obtained when $Fe(CO)_5$ was used. The total HNCs mean size was found to not vary significantly with respect to sample **HNCs_CO**, while the iron oxide domain was found to be reduced down to ~7 nm. Undesirably, a secondary consistent population of single iron oxide NCs (~6.5 nm) was also obtained, as a consequence of a simultaneous occurrence of homogenous and heterogeneous nucleation process.

The different results obtained from the two different iron precursors suggest a different nucleation/growth regime arising from their different chemistry and reactivity. It is well known that the formation of iron oxide NCs when starting from a $Fe(CO)_5$ precursor occurs through the initial formation of metallic Fe NCs and their posterior oxidation,[36] while iron oxide NCs are directly obtained with the $Fe(acac)_3$ precursor.[37] Similarly, in the seeded-growth synthesis of Au-Fe_3O_4 HNCs starting from $Fe(CO)_5$ the mechanism proposed is the initial nucleation of the intermediate Fe metallic phase onto the Au NCs surface,[16,38] followed by oxidation. In addition, it has been reported that $Fe(CO)_5$ experiences a delayed sudden nucleation when injected in solution in the presence of carboxylic acids surfactants,[39] which complex the Fe(0) and prevents the rapid nucleation of Fe nanoparticles. Subsequently, as the temperature is raised the formed complex decomposes, leading to a burst nucleation. This mechanism suggests that, using $Fe(CO)_5$ in the presence of Au NCs, the heterogeneous nucleation onto the gold surface and the successive growth of the resulting iron domain are strongly favored with respect to the homogeneous nucleation, resulting in the strong preference to form dimer-like structures. Similarly, $Fe(acac)_3$ is also reported to form intermediate complex, related with the complexation of Fe(III) with oleic acid and oleylamine ligands.[40] However, in this case the strong prevalence of heterogeneous nucleation over the homogeneous one does not occur, resulting in a mixture of

single Fe_3O_4 NCs and Au-Fe_3O_4 HNCs, the latter ones having isotropic flower-like and incomplete core-shell morphologies.

These results suggest also that the optimal conditions for the formation of Au-Fe_3O_4 HNCs have to be tuned depending on the iron precursor used. In the literature, the synthetic protocols for the synthesis of iron oxide NCs from $Fe(acac)_3$ includes two additional features: the presence of a step at intermediate temperature (200-205 ºC) during a prolonged time (>30 min), in order to promote the formation of the complex of Fe(III) with surfactants, and the use of a long chain diol (1,2-hexadecandiol or 1,2-dodecanediol).[34,41] These molecules have been reported to act as accelerant in the formation of the Fe-O-Fe bonds and as mild reducing agents, acting in addition as co-surfactants.[34,42] In view of these, the reaction based on $Fe(acac)_3$ was reformulated modifying the conditions in order to fulfill the above requirements. The ratio between the reactants reported by Roca *et al.*[43] was used, although testing different solvent volumes (from 20 to 50 mL) with the aim to promote the heterogeneous nucleation by lowering the iron concentration. Indeed, the homogenous nucleation is expected to occur in supersaturation conditions, while in the presence of Au NCs as seeds, the heterogeneous one should occur even at lower precursor concentration.[44] From the TEM images (**Figure 3b-c** and **Figure S6**), it can be clearly seen that the heterogeneous nucleation is promoted over the homogenous one with the increase of total reaction volume, as expected, by bringing the iron precursor under the supersaturation threshold.

Following this strategy, monodisperse Au-Fe_3O_4 HNCs with dimer morphology (**HNCs_acac**, **Figure 2b** and **Figure 3c**) could be obtained also from the thermal decomposition of the $Fe(acac)_3$ precursor, by modifying the reaction parameters and increasing the reaction volume up to 50 mL. TEM characterization shows that even if the sample is composed by almost single iron

oxide domain HNCs (about 70%), a secondary population of Au NCs with multiple iron oxide domains (up to a maximum of 4) is also present. The morphology of the iron oxide domains is found to be more irregular compared to **HNCs_CO**, but with similar size (around 9 nm), while the total mean size of the HNCs is about 23 nm. Again, no significant variation of the gold domain with respect to the starting Au NCs was observed (**Figure S5**), in concordance with the **HNCs_CO** case.
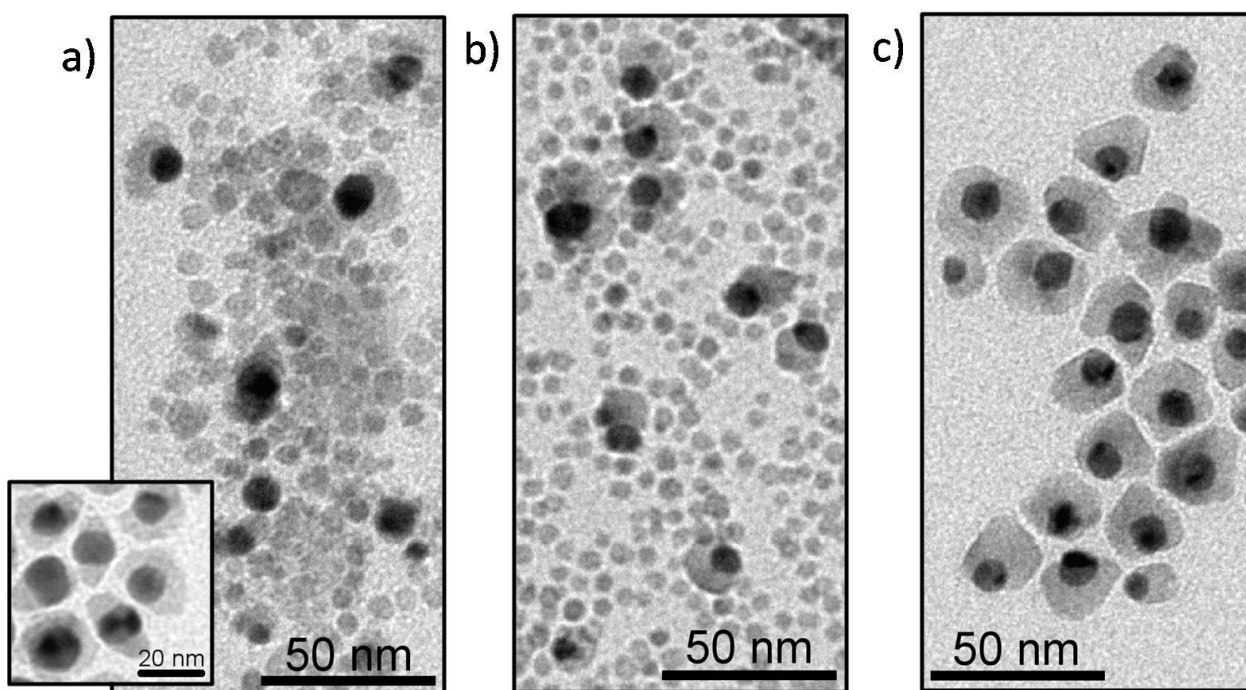

Figure 3: Representative TEM images of Au-Fe$_3$O$_4$ HNCs obtained from the Fe(acac)$_3$ precursor in different conditions: a) Same reaction conditions as for **HNCs_CO**. In the inset is reported a magnification of the obtained HNCs; b) Modified reaction conditions, with the introduction of 1,2-dodecanediol and a step of 2 h at 200 ºC; c) Effect of the increase of the reaction volume to 50 mL.

Effect of the [Fe]:[Au] ratio. Although tuning the [Fe]:[Au] molar ratio is also expected to affect the nucleation of iron oxide NCs, interestingly, it also influences the morphology of the HNCs. Indeed, in the case of Au-Fe$_3$O$_4$ HNCs obtained using Fe(CO)$_5$, the presence of a significant secondary population with flower-like morphology (about 35%) was observed when [Fe]:[Au] ratio changed from 2 to 9 (**Figure 4a**). Notably, the absence of isolated iron oxide NCs

13

and the high amount of dimers still present suggests that even in the presence of higher iron precursor concentration, heterogeneous nucleation and growth is still preferred. As a consequence, the higher amount of iron precursor available and its affinity for the Au NC surface will lead to multiple heterogeneous nucleations on the surface of Au NCs.

On the other hand, in the case of $Fe(acac)_3$, taking as reference a total volume of 20 mL, the reduction of the [Fe]:[Au] ratio from 10 to 3 strongly inhibits the formation of single iron oxide NCs (down to about 5%), leading to a mixture of dimer HNCs with different sizes and shapes, and some isolated Au NCs (**Figure 4b**). Thus, by controlling the amount of iron present in the reaction it is possible to act on the supersaturation conditions, strongly hampering the homogenous nucleation and promoting the heterogeneous nucleation of iron oxide phase on the Au surface.
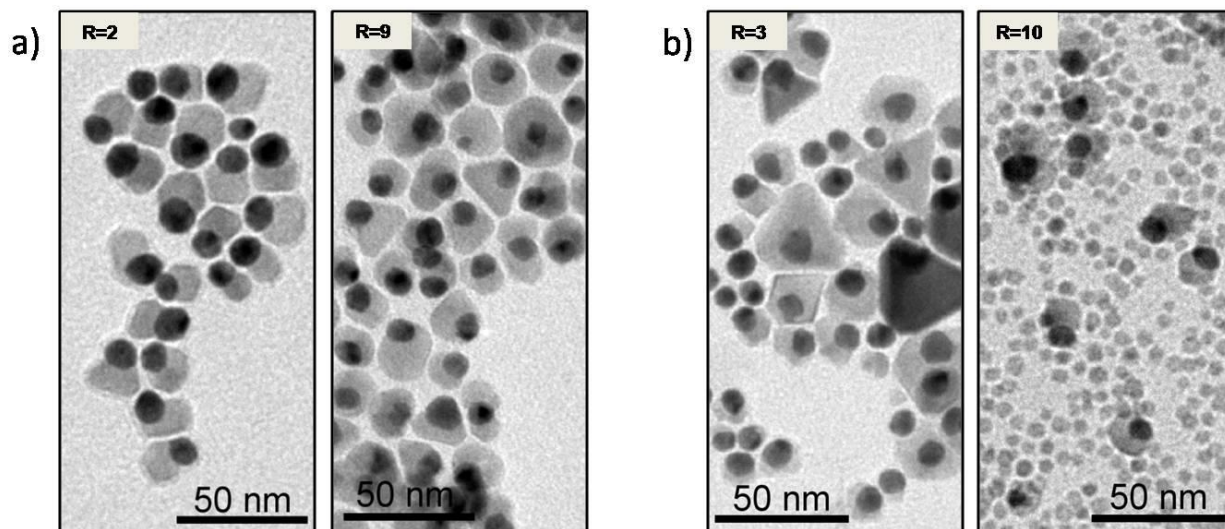

Figure 4: Representative TEM images of Au-Fe_3O_4 HNCs obtained from the $Fe(CO)_5$ (a) and $Fe(acac)_3$ (b) precursor using different [Fe]:[Au] precursors molar ratio (R).

Effect of the composition of the Au NCs coating layer. In the synthesis of inorganic NCs by thermal decomposition, surfactants play a key role participating in the formation of the

intermediate complex,[40,42] protecting the surface and confining the size of the obtained nanostructures to the nanoscale. Surfactants form a dynamic layer/barrier on NCs, which allows not only controlling the growth of the NCs by itself but also the nucleation of another inorganic phase onto their surface. Thus, the modification of the composition of the surfactant layer of the Au NCs used as seeds is it known to have also an important role in the formation of Au-Fe_3O_4 HNCs. Accordingly, Schick *et al.*[21] reported that coating the Au NCs with long chain thiols inhibits the heterogeneous reaction, while coating it with oleylamine enables the seeded-growth reaction.

In order to understand how the difference in composition of the surfactant mixture affects the composition and structure of the coating layer of the Au NCs and consequently the accessibility to the surface for heterogeneous nucleation, the reaction was repeated for both precursors using two different Au NCs obtained in the presence of oleylamine and 1,2-dodecanediol[17] (**Au NCs_A,**) in one case, and with only oleylamine[45] (**Au NCs_B**) in the other case. The obtained Au NC seeds have similar size and show the same structural and optical properties (**Table S1**). In particular, high resolution TEM images (**Figure S2 c-d** and **S3 c-d**) show that both are composed of multiply twinned NCs, a particular feature typical for Au NCs obtained from reduction oleylamine in organic solvents.[17,46]

In the case of $Fe(CO)_5$, an increase of the HNCs size (from ~22 nm to ~28 nm) and variations in HNCs morphology were observed moving from **Au NCs_A** (**Figure 5a**, left) to **Au NCs_B** (**Figure 5a**, right). On the other hand, in the case of $Fe(acac)_3$ no significant differences were observed in the obtained HNCs (**Figure S7**), even if the product obtained from **Au NCs_A** (**Figure S7a**) shows the presence of a secondary population of single iron oxide NCs of ~ 9 nm. These results indicate that the presence of 1,2-dodecanediol in the coating layer of the Au NCs

has a significant effect on the reaction, with different results depending on the iron oxide precursor considered. Note that one could expect that amines will compete successfully for the Au NC surface. However, as lability of functional groups decreases with increasing molecule chain length, the short di-alcohol can thus compete efficiently for the longer amine terminated molecule. In the case of $Fe(CO)_5$, the presence of 1,2-dodecanediol presence influences the final morphology of HNCs, suggesting that this molecule acts mainly as templating agent, controlling the growth of the iron oxide phase or limiting its access to the Au NCs surface. On the other hand, the presence of a secondary population of iron oxide NCs obtained from **Au NCs_A** and $Fe(acac)_3$, absent using **Au NCs_B**, suggests that in this case the 1,2-dodecanediol actively participates in the reaction, promoting homogenous nucleation of iron oxide, in concordance with its role of accelerant in the formation of the Fe-O-Fe bonds reported in the literature.[34,42] Therefore, on the basis of the obtained experimental results, the most suitable coating for Au NCs was chosen depending on the iron precursor used, i.e. oleylamine and 1,2-dodecanediol (**Au NCs_A**) for $Fe(CO)_5$ and only oleylamine (**Au NCs_B**) for $Fe(acac)_3$.
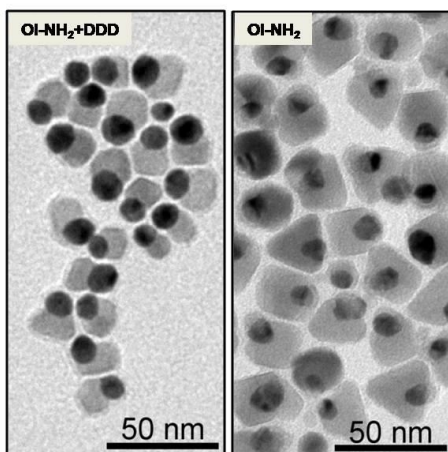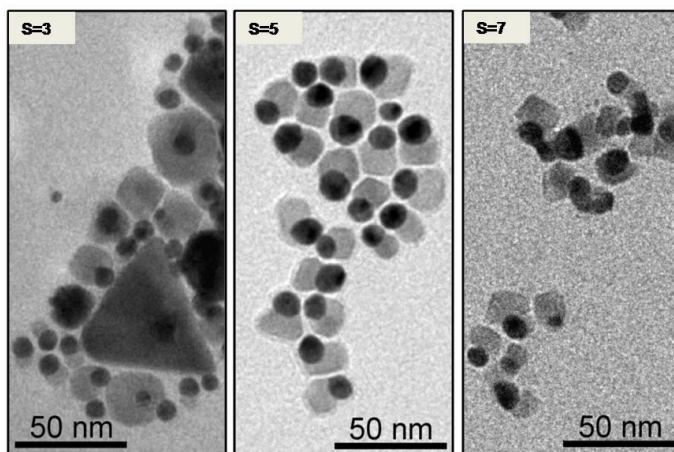

Figure 5: Representative TEM images of Au-Fe_3O_4 HNCs obtained from the $Fe(CO)_5$ precursor by changing the reaction conditions.

Effect of the amount of surfactant. For the $Fe(CO)_5$ precursor, the effect of the amount and the nature of the employed surfactants on the HNCs formation and morphology was investigated. In the presence of only oleic acid with a [Fe]:[oleic acid] ratio of 1:3 (**Figure S8a**) a product composed of large aggregates is obtained. On the other hand, when using only oleylamine with a [Fe]:[oleylamine] ratio of 1:3, inhomogeneous HNCs with different morphologies were observed (**Figure S8b**), together with single iron oxide NPs. Consequently, in a second set of experiments the effect of [surfactant]:[iron] molar ratio on the formation of HNCs was also investigated using the ratios of 3, 5 and 7 (**Figure 5b**). Au-Fe_3O_4 HNCs with a single iron oxide domain were observed for all the ratios tested, however, the product with the best characteristics in terms of morphology and size distribution was obtained with a ratio of 5. The obtained data shows how the degree of protection of the seed NCs surface, a dynamic coating strong enough to avoid aggregation but weak enough to allow the seeded-growth process, can be modulated by varying the composition and the amount of surfactants in the reaction mixture, as much as the temperature (vide infra). Indeed, both oleylamine and oleic acid are necessary for obtaining well-formed and homogeneous Au-Fe_3O_4 HNCs, playing respectively a primary role against aggregation and in the control of size distribution of the iron oxide domains, respectively. Thus, in the presence of low amount of surfactant ([surfactant]:[iron] of 3) a lack of control over the growth process is observed, while with an excess of surfactant ([surfactant]:[iron] of 7) the control of the morphology is weak.

Effect of the reaction temperature. Another way to control the seeded-growth nucleation process is acting on the reaction temperature. With the decrease of temperature in the presence of Au NCs seeds, it has been proposed that the heterogeneous nucleation will be favored at the expense of the formation of new nuclei, a process that requires the overcoming of a greater

energy barrier than growth.[47] In order to investigate this aspect, the effect of the decrease of the reaction temperature was investigated for both precursors. Unexpectedly, in the case of Fe(acac)$_3$, taking as reference a total volume of 20 mL and 0.15 mmol of iron precursor (**Figure 6a, *left***), the decrease of the temperature reaction from 315 to 290 ºC led to homogenous nucleation of Fe$_3$O$_4$ NCs, with the complete absence of Au-Fe$_3$O$_4$ HNCs (**Figure 6a, *right***). The observed data suggests that in these conditions the temperature was not high enough for the growing iron oxide phase to overcome the energy barrier imposed by the oleylamine coating the Au NCs surface, leading to a complete lack of heterogeneous nucleation. To confirm this hypothesis, the reaction was repeated reducing the concentration of free oleylamine from 2 to 0.2 mmol (**Figure 6b**). In these conditions, the process of homogenous nucleation was almost completely inhibited and a population of flower-like HNCs of ~37 nm was obtained (**Figure 6b**). Furthermore, the complete removal of free oleylamine from the reaction mixture has a detrimental effect, leading to the coalescence of Au NCs (**Figure 6b**), indicating that this molecule has a key role in the stabilization of Au NC and controlling access to its surface. Moreover, as the amount of free oleylamine is reduced, a modest increase of the mean size of the gold domain of HNCs was observed with respect to the original Au NCs, that can be ascribed to Ostwald ripening, to a further reduction of Au precursor or to atomic rearrangement occurring during the reaction at high temperature.

In this regime of low oleylamine concentration (0.2 mmol), a further reduction of the reaction temperature to 270 ºC leads to a double population of single Au and small (~5 nm) iron oxide NCs (**Figure 6c**) evidencing again the lack of sufficient thermal energy to overcome the surfactant layer (as temperature decreases the NC-surfactant bond hardens and the equilibrium between surfactant molecules at the surface of the NCs and in solution is slowed down).

Interestingly, using a solvent with higher coordination capacity for the Fe-carboxylate complex such as benzyl ether (Bz$_2$O), flower-like HNCs with a total mean size around 37 nm (**Figure 6c**) could be obtained. Besides, the use of a lower boiling point solvent such as phenyl ether (Ph$_2$O, b.p. 260 ºC) makes the iron oxide domain smaller (**Figure 6c**), indicating that, if conditions for heterogeneous nucleation are optimized, iron oxide domains can be easily tuned by decreasing the boiling point, a behavior already reported in the literature on single magnetite NCs synthesized by thermal decomposition.[48] Interestingly, when different solvent mixtures [i.e., 1-octadecene (ODE) and phenyl ether (Ph$_2$O) with ratio 3:1, 1:1 and 1:3)] were tested keeping a constant reaction temperature (265-270 ºC), a mixture of HNCs with different morphologies were obtained (**Figure 6c**), with the percentage of HNCs with a single iron oxide domain increasing with the amount of phenyl ether reaching a maximum of ~50% in the case of the ODE:Ph$_2$O ratio 1:3 (**Figure 6c**). On the other hand, in the case of the Fe(CO)$_5$ precursor a reduction of the temperature to 290 ºC leads to the complete absence of iron oxide NCs in the final product (**Figure S9a**), indicating that these conditions are not sufficient for the formation of the iron oxide phase. This is supported by the presence of low contrast amorphous material around the Au NCs which can be identified as the intermediate iron-surfactant complex.[39] However, similarly to what is observed with the Fe(acac)$_3$ precursor, when the reaction was repeated using benzyl ether (Bz$_2$O, b.p. 285 ºC) well-defined HNCs were obtained **Figure S9b**). The overall results for the Fe(acac)$_3$ and Fe(CO)$_5$ precursors indicate that the nature of the solvent plays a key role in the nucleation of the iron oxide phase. The solvent determines the physical properties of the reaction surrounding media (i.e. polarity, viscosity, density) and strongly influences the solubility and the stability of the different reactants and the intermediate species, thus having a significant effect on the outcome of the reaction.
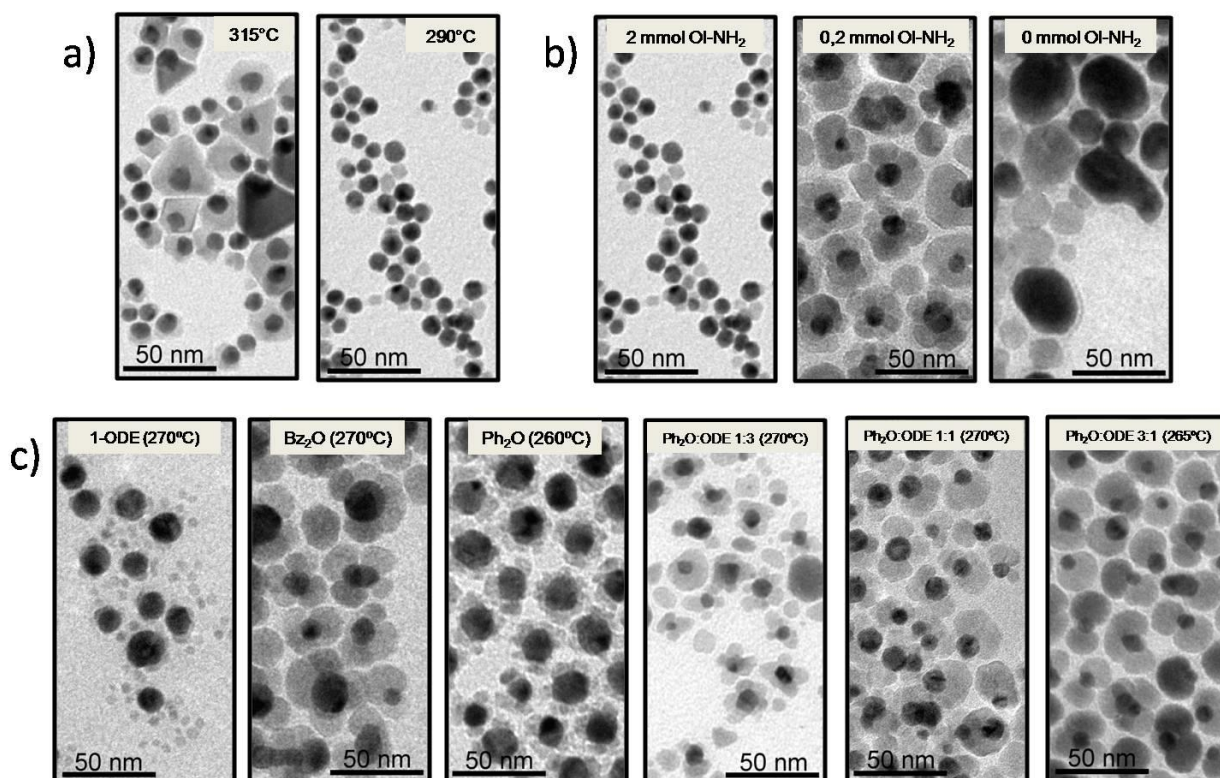
Figure 6: Representative TEM images of Au-Fe$_3$O$_4$ HNCs obtained from the Fe(acac)$_3$ precursor in different conditions: a) Effect of the reaction temperature in 1-octadecene; b) Effect of the reduction of the oleylamine (Ol-NH$_2$) amount in 1-octadecene at 290°C; f) Effect of the reaction solvent (with 0.2 mmol of Ol-NH$_2$).

Control of the growth of the Fe$_3$O$_4$ domains. Once the synthetic conditions leading to the heterogeneous nucleation of the iron oxide onto the Au NCs surface are well established, the second step is the investigation of the parameters that influence the growth of the formed iron oxide phase. Controlling the size of the iron oxide moiety is important since it has a critical effect on the magnetic properties of the final material.

Primarily, a parameter that is expected to control the mean size of the iron oxide phase is the amount of iron precursor. However, in the case of Fe(CO)$_5$ no significant differences in the mean size of the obtained HNCs with dimer morphology (~20 nm) were observed when the [Fe]:[Au] ratio was varied from 1.6 to 9.3: the mean size of the iron oxide domain was found to be constant around 10 nm. The principal effect of the use of an higher [Fe]:[Au] ratio was the rising of a

secondary population (up to 36%) of HNCs with more than one iron oxide domain, with total mean size slightly larger (~26 nm) (**Figure 4a**). In the case of Fe(acac)$_3$, the higher tendency to form isolated iron oxide NCs (homogeneous nucleation) with the increase of iron precursor concentration strongly conditions the investigation of the possible effects of the [Fe]:[Au] ratio. Besides, in the regime of reduced concentration of free oleylamine, it was observed that the reduction of the [Fe]:[Au] ratio from 2.5 to 1.6 (**Figure S10**) leads to a reduction of the mean iron oxide phase from ~ 10 nm to 5 nm. Additionally, still for Fe(acac)$_3$, the analysis of the obtained data shows that the mean size of the iron oxide domain can also be influenced by the reaction temperature. For example, Au-Fe$_3$O$_4$ HNCs obtained from Fe(acac)$_3$ at 260 °C in phenyl ether show iron oxide domains significantly smaller (5 nm) with respect to the sample obtained at 270 ºC in benzyl ether (~ 11 nm) (**Figure 6c**). Moreover, the variation of the coordination capacity of the solvent, while keeping constant the reaction temperature to 270 ºC, was found also to slightly affect the final iron oxide size domain. Indeed, using different solvent mixtures of 1-octadecene and phenyl ether (3:1, 1:1 and 1:3), the iron oxide domain size was found to increase with the polarity of the final solvent mixture, going from about 7 nm in the case of ODE:PhO ratio 3:1 to about 11 nm in the case of ODE:PhO ratio 1:1 and 1:3 (**Figure 6c**).

HNCs characterization. In **Figure 7a** are reported the powder XRD patterns of Au-Fe$_3$O$_4$ HNCs with dimer morphology synthesized using different precursors (**HNCs_CO** and **HNCs_acac**). In both cases, two phases were identified, matching the reference patterns of gold (PDF-00-004-0784) and of magnetite (PDF-00-019-0629) or maghemite (PDF-00-039-1346), and no evidence of any additional inorganic phase was observed. The lattice parameters, a, reported in Table 1, were found to be in excellent agreement with the reference values of magnetite (8.3919Å) and gold (4.0786Å). The mean crystalline size of Au domains (Table 1),

estimated with the Scherrer analysis on the (111) diffraction peak was found to be smaller with respect to the mean size obtained from TEM: this behavior was already observed in the case of the Au NCs seeds (see SI) and can be ascribed to the polycrystalline multiple-twinned structure of nanosized gold. On the other hand, in the case of the iron oxide domains, due to their irregular shape, the direct comparison between the obtained values is more complex: the mean crystalline size found for the magnetite phase, estimated on the (311) diffraction peak, was found to be higher with respect to the TEM reported mean size for both samples.
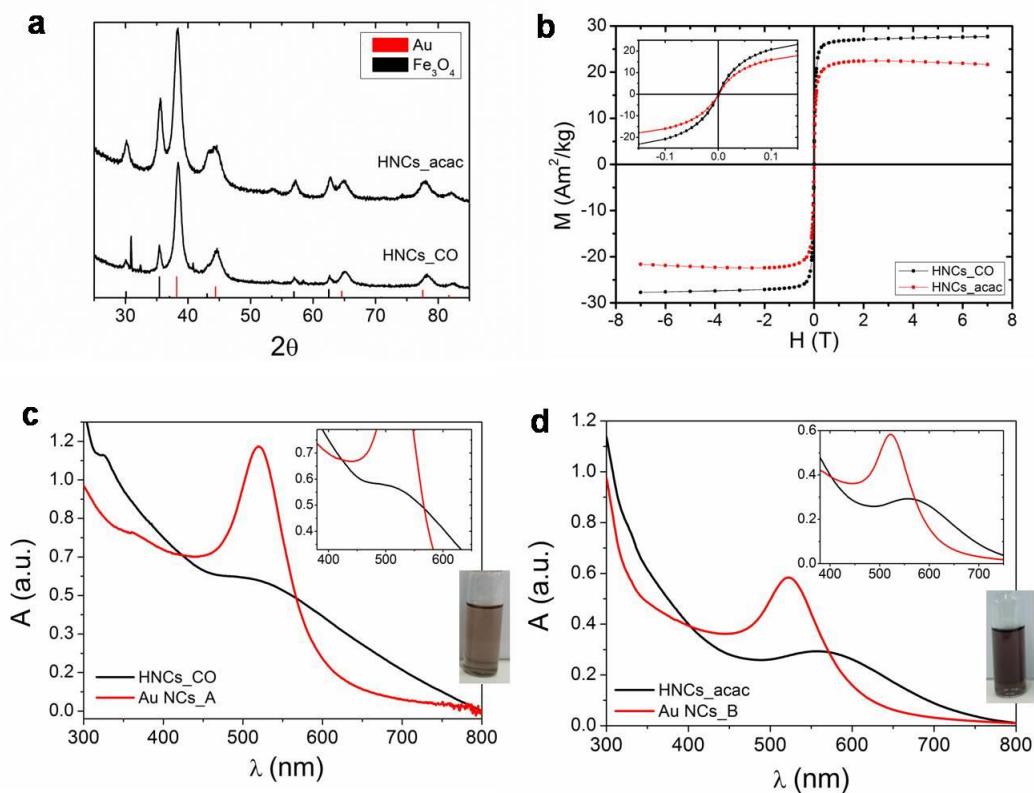

Figure 7: a) X-ray diffraction patterns of the **HNCs_CO** and **HNCs_acac** samples. The black and red bars correspond to the reference pattern for magnetite (PDF-00-019-0629) and gold (PDF-00-004-0784), respectively. b) Magnetization curves of the **HNCs_CO** and **HNCs_acac** samples recorded at 300 K. Shown in the inset is the magnification of the low field region. c,d) UV-VIS spectra of **HNCs_CO** (c) and **HNCs_acac** (d) compared with the corresponding Au NCs used as seeds. Shown in the inset are the magnifications of UV-VIS spectra and the photograph of the respective sample dispersions in hexane.

Table 1: Structural and optical properties of Au-Fe$_3$O$_4$ HNCs.

Sample	HNCs	Fe$_3$O$_4$ domain				Au domain			HNCs
	d_{TEM} (nm)	d_{TEM} (nm)	a (Å)	d_{XRD} (nm)	d_{TEM} (nm)	a (Å)	d_{XRD} (nm)	λ_{max} (nm)
HNCs_CO	22 ± 4	10± 2	8.391(3)	20 (1)	12± 2	4.058(1)	9.18 (0.08)	~520
HNCs_acac	23 ± 3	9 ± 3	8.392(3)	13.8 (0.5)	11 ± 2	4.074(1)	7.7 (0.1)	557

d_{TEM}: HNCs average diameter and standard deviation obtained from TEM analysis; a, d_{XRD}: lattice parameter and crystallite mean size obtained from XRD data analysis (errors are reported in brackets); λ_{max}: wavelength of the plasmonic resonance.

In order to have a better insight of HNCs structure at the nanoscale, a detailed high resolution TEM (HR-TEM) characterization was performed (**Figure 8**). In the two types of samples, a high crystallinity of both the Au and iron oxide domains was observed (**Figure 8c,f**). The gold domains showed the usual metallic gold cubic Fd$\overline{3}$m crystal lattice (although with planar defects; **Figure S11**), whereas the iron oxide moiety presents a cubic spinel structure (space group Fd3m) consistent with Fe$_3$O$_4$ (**Figure 8b,e**). The most commonly observed relative orientations between Au and Fe$_3$O$_4$ are compatible with (100)[010]$_{Au}$//(100)[010]$_{Fe3O4}$ epitaxial relations (**Figure S11**). This indicates that a unit cell of magnetite (lattice parameter 8.4Å) is matched by 2x2 gold unit cells (lattice parameter 4.1Å), which translates into a lattice mismatch of 2.8%. Note that relative orientations with [100]Au zone axis parallel to [112]$_{Fe3O4}$ are also occasionally seen (see **Figure S11**). Importantly, no significant differences have been detected between the **HNCs_CO** and **HNCs_acac** samples. An Electron Energy Loss Spectroscopy (EELS) study was also carried out, with the aim to investigate the elemental composition and the homogeneity of the two different phases in the HNCs. The spectrum images (**Figure 9**) clearly show that for both synthesis approaches the two phases are separated by a very sharp interface without interdiffusion. Interestingly, the relative composition Fe signal/(O signal+Fe signal) is constant

along the iron oxide domain (**Figure 9c,i** and **Figure S12**), indicating an homogeneous composition of the iron oxide counterpart. The analysis of the fine structure of the EELS spectra[49] (**Figure 9f,n** and **Figure S12e**) shows that they are equivalent to that of magnetite, Fe_3O_4, reference spectrum.[50] Additionally, no changes in the oxidation state were detected in the sample, thus, the presence of a secondary phase of metallic Fe or FeO can be excluded **Figure S12d,e**).
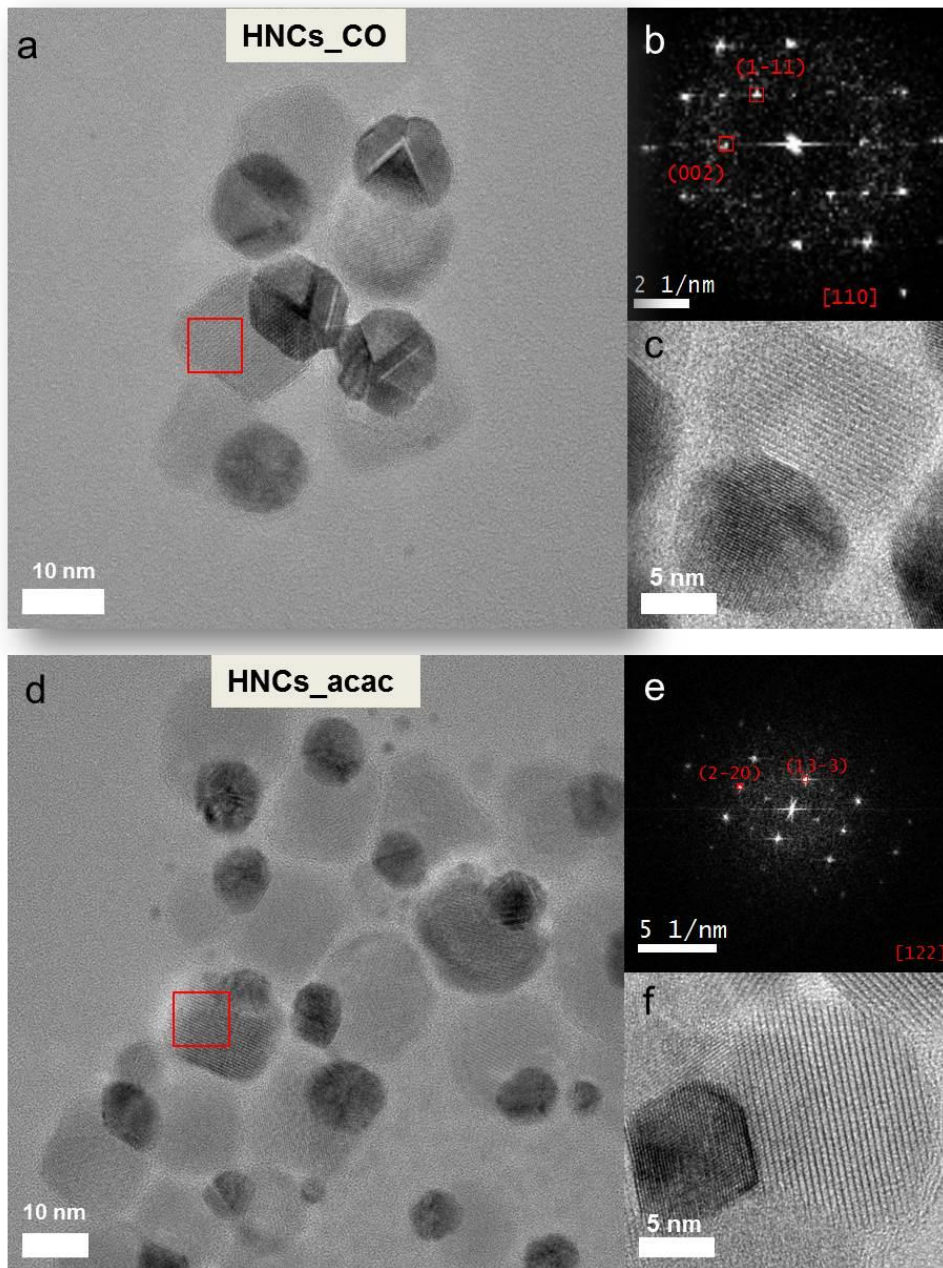
Figure 8: High Resolution images (a,c,d,f) and Fast Fourier Transform (FFT) (b,e) of samples **HNCs_CO** (a,b,c) and **HNCs_acac** (d,e,f). The FFT was taken from the region highlighted in red in HRTEM images (a,d).
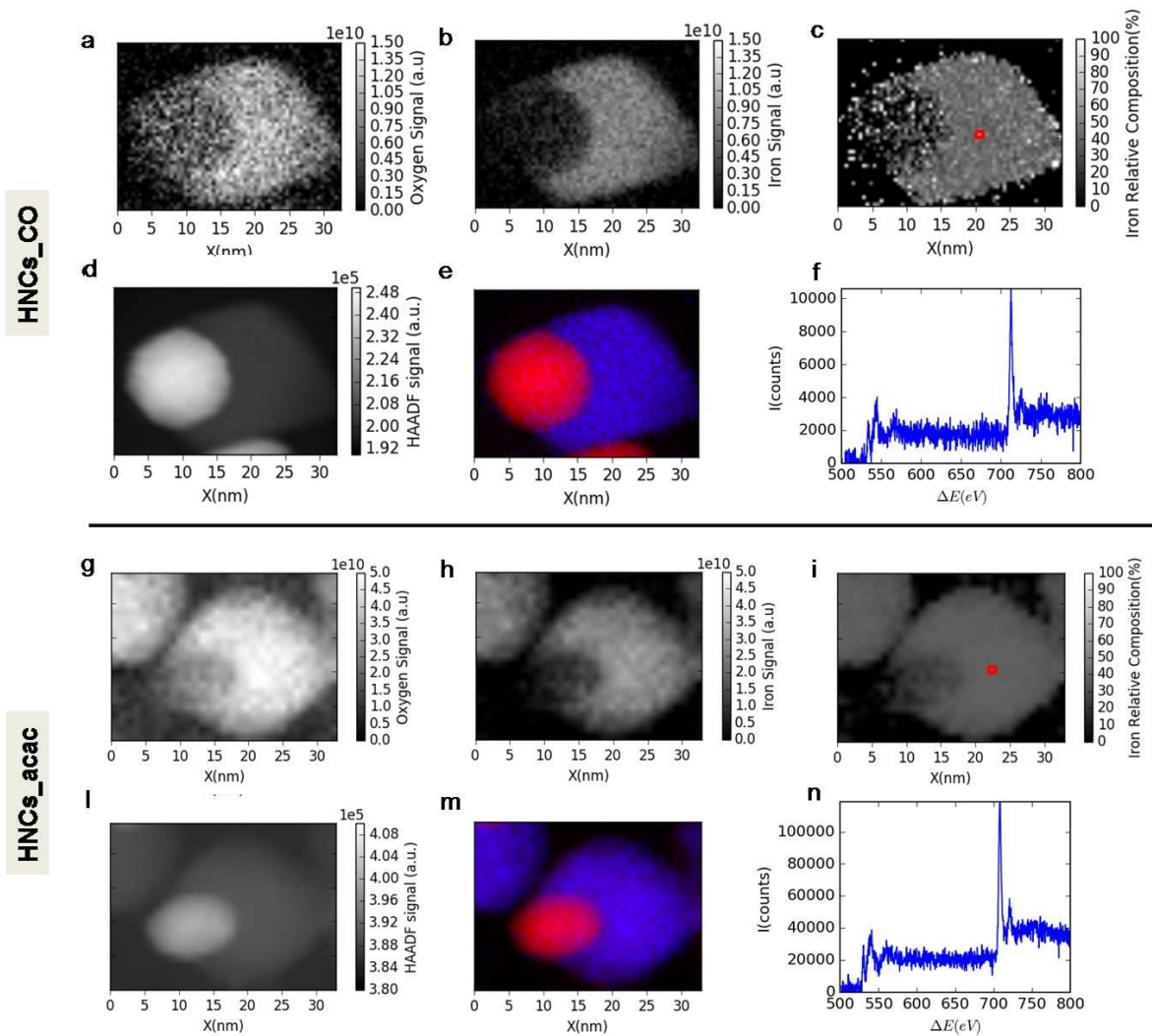
Figure 9: EELS spectrum imaging of samples **HNCs_CO** (a-f) and **HNCs_acac** (g-n). a, g) O K-edge signal; b, h) Fe L-edge signal; c, i) relative iron composition Fe signal/(O signal + Fe signal); d, l) HAADF co-acquired signal; e, m) HAADF + Fe signal color mix (Fe L-edge signal in blue, background in red); f, n) experimental EELS spectra at the position corresponding to the red dot in relative composition panel (c and i, for **HNCs_CO** and **HNCs_acac**, respectively).

Concerning magnetic properties, it is worth to note that at room temperature both samples exhibit a ferromagnetic behavior with very small coercivity, H_C. The low saturation magnetization (M_S) values observed per mass of HNCs (28 and 22 Am^2kg^{-1} for samples **HNCs_CO** and **HNCs_acac**, respectively) rescale to those commonly reported in the literature for nanosized iron oxide (60-80 Am^2kg^{-1}) once the effective weight percentage of the iron oxide phase is estimated. On the other hand, at low temperature (10 K) both samples show open

hysteresis loops (**Figure S13**) with coercivity values (**Table S2**) consistent with the data reported in the literature for HNCs with similar size.[27] The temperature dependence of the magnetization, *M(T)*, of both samples cooled in the absence (Zero Field Cooled, ZFC) or the presence (Field Cooled, FC) of a magnetic field of 2.5 mT (**Figure S13**) shows the thermal irreversibility typical of nanosized magnetic materials. The shape of *M(T)*, with a rather flat FC *M(T)*, is typical of strongly interacting magnetic nanoparticles. Interestingly, the blocking temperature, T_B, is clearly above room temperature. Thus, T_B is somewhat high compared to Fe_3O_4 particles of similar sizes,[51,52] even taking into account dipolar interactions. The possible origin of such enhanced T_B are manifold, e.g., shape effects, strain effects (due to the lattice mismatch), or even charge transfer at the Au-Fe_3O_4 interface.[27,53–56]

The optical properties of the obtained Au-Fe_3O_4 HNCs were investigated by UV-VIS absorption spectroscopy. In the case of **HNCs_CO**, the spectrum shows a strong damping of the plasmon resonance peak with respect to the starting Au NCs, with no significant shift of the maximum wavelength (**Figure 7**c). On the other hand, **HNCs_acac** shows the presence of a well-defined plasmonic peak (although broader than the corresponding Au seeds) shifted towards higher wavelengths (557 nm) with respect to the starting Au NCs (519 nm). Both red shift and damping of the plasmonic peak are phenomena commonly observed in Au-Fe_3O_4 HNCs[16,17,21,31,57] and are related to the presence of the iron oxide in direct contact with the Au domain. Au NCs are very sensitive to the refractive index of their surroundings,[58] therefore the high refractive index and absorption of Fe_3O_4 can induce optical changes in the HNCs, which increase as the Au NCs surface is covered by the iron oxide. Consequently a sample with inhomogeneous iron oxide coverage will lead to both red shift and broadening of the plasmonic

band. On the other hand, the high absorption of the iron oxide generates additional broadening of the plasmonic band due to the damping of the localized plasmonic resonance in the Au NCs.[56]

The different optical behavior observed in **HNCs_CO** and **HNCs_acac** samples can be explained considering the differences in surface coverage of Au NCs by iron oxide. By comparing the TEM images (**Figure 2**) it can be noticed that in the case of **HNCs_acac** the Au domain is surrounded by a higher amount of iron oxide with respect to **HNCs_CO**. In the latter, a large portion of the Au is exposed to the external environment and the Au-iron oxide interface is less extended with respect to **HNCs_acac**, resulting thus in a lower red shift. Moreover, the peculiar morphology of **HNCs_CO** sample can favor the inter-particle interactions between different Au domains: this phenomenon can favor the near-field interaction between the plasmonic parts in the HNCs, which can induce additional broadening of the plasmonic peaks.

Silica coating

For the application of Au-Fe$_3$O$_4$ HNCs in the biomedical field (e.g., as contrast agents for imaging or as multifunctional heat mediators for hyperthermia) a successive step of transfer and stabilization in water media is needed. For this purpose, a simple, solid and robust strategy is the encapsulation of the HNCs in amorphous silica. The dimer Au-Fe$_3$O$_4$ HNCs were thus transferred to water using a reverse-emulsion method[57,58] (see Experimental Section). The Si precursor (TEOS) is hydrolyzed around each HNCs inside reverse micelles, which have the role in controlling the size of the final coating. As it can be observed in **Figure 10**, the Au-Fe$_3$O$_4$ HNCs were successfully encapsulated by a spherical silica shell, reaching an overall diameter of around 60 nm, without any alteration of HNCs morphology and size.
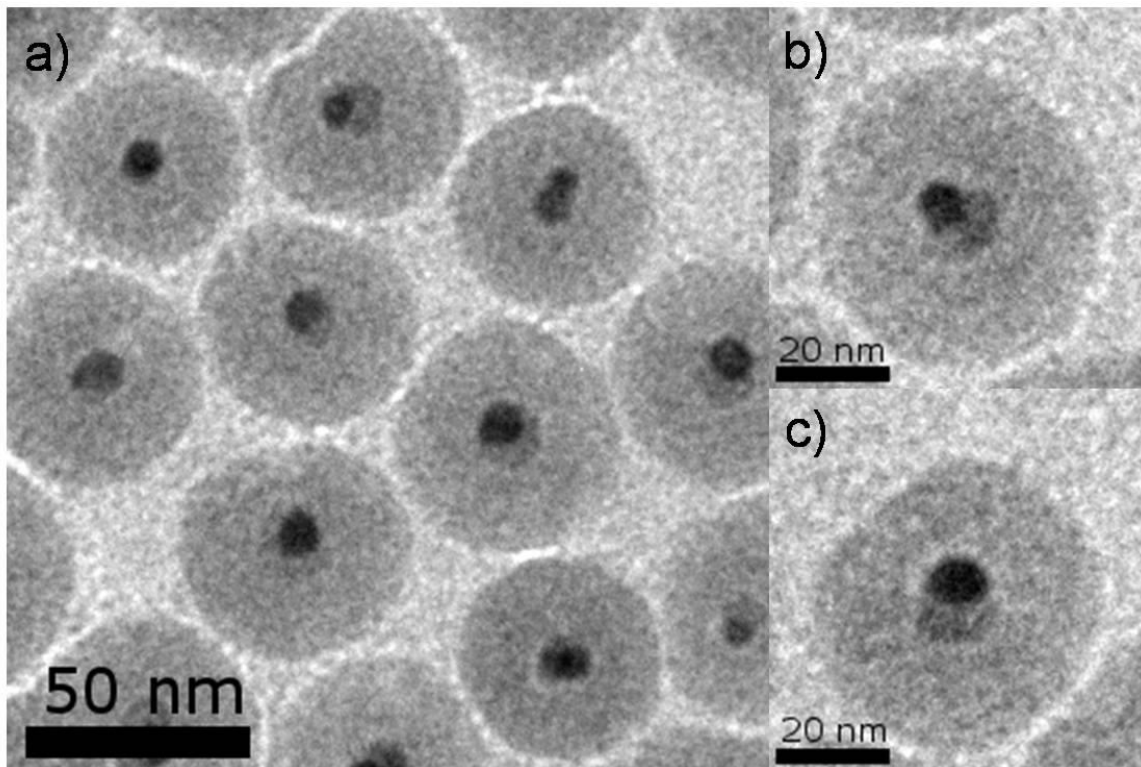
Figure 10: Representative TEM image of sample **HNCs_CO@SiO₂** (a) and magnification of single particles (b,c).

Conclusions

In conclusion, well defined Au-Fe$_3$O$_4$ HNCs (dimers or flower-like morphologies) were obtained by seeded-growth on preformed oleylamine-capped Au NCs using two different iron precursors, Fe(CO)$_5$ and Fe(acac)$_3$. Depending on the iron precursor used, the reaction conditions have to be varied in order to promote the heterogeneous nucleation and, thus, to obtain a single type of HNCs. The results suggest that a different nucleation/growth regime occurs in relation to the different chemistry and reactivity of the precursors. The synthetic strategy based on the thermal decomposition of Fe(CO)$_5$ precursor was found to be reproducible, robust and effective for obtaining monodisperse Au-Fe$_3$O$_4$ HNCs with dimer morphology, with a single nucleation of iron oxide domain for each Au seed. The study on the reaction parameters suggests that both oleic acid and oleylamine play an important role in the formation of well-defined HNCs and their

amount with respect to iron helps in controlling the size distribution, with an optimal [surfactant]:[iron] ratio of 5. The increase of the [Fe]:[Au] ratio was found to have effect on the morphology of the obtained HNCs, leading to a mixture of dimer and flower-like HNCs. Moreover, it was observed that a minimum reaction temperature, which depends on the kind of solvent used, is required in order to observe the formation of HNCs.

On the other hand, the reaction performed using $Fe(acac)_3$ as precursor was found to be much more sensitive to the change of the reaction parameters. Well-defined monodisperse HNCs with dimer or flower-like morphologies can be obtained only using specific conditions that promote the heterogeneous nucleation, i.e. a large amount of solvent, the reduction of the [Fe]:[Au] ratio or the reduction of the amount of free oleylamine in the reaction mixture. Indeed, oleylamine was found to have a key role in regulating the accessibility to the Au NCs surface, favoring the heterogeneous nucleation process when reduced but leading to Au NCs sintering if completely eliminated. Unlike to what has been previously observed with the $Fe(CO)_5$ precursor, the presence of more than one nucleation point on Au NCs surface suggests a lower selectivity of the heterogeneous nucleation process. The mean size of the obtained HNCs can be tuned by varying the [Fe]:[Au] ratio, which in turn has to be low enough in order to not overcome the supersaturation threshold and to avoid undesired homogenous nucleation processes. Finally, the solvent used was found also to have a significant effect on the formation of the iron oxide domains, resulting in variations of HNCs morphology.

SUPPORTING INFORMATION.

TEM images, Powder X-Ray diffraction patterns and UV-VIS spectra of Au NCs; TEM image of a mix of Au and Fe_3O_4 HNCs; histograms of Au NCs and HNCs Au domains obtained from TEM images; additional TEM images of $Au-Fe_3O_4$ HNCs; additional High Resolution TEM

images and Fast Fourier Transform of Au-Fe$_3$O$_4$ HNCs; Electron Energy Loss Spectroscopy spectrum and spectrum images of Au-Fe$_3$O$_4$ HNCs; Zero Field Cooled and Field Cooled magnetization and hysteresis loops at 10 K of Au-Fe$_3$O$_4$ HNCs; detailed synthetic procedures for all the samples presented. This material is available free of charge via the Internet at http://pubs.acs.org.

REFERENCES

(1)   Cozzoli, P. D.; Pellegrino, T.; Manna, L. Synthesis, Properties and Perspectives of Hybrid Nanocrystal Structures. *Chem. Soc. Rev.* **2006**, *35* (11), 1195–1208.

(2)   Carbone, L.; Cozzoli, P. D. Colloidal Heterostructured Nanocrystals: Synthesis and Growth Mechanisms. *Nano Today* **2010**, *5* (5), 449–493.

(3)   López-Ortega, A.; Estrader, M.; Salazar-Alvarez, G.; Roca, A. G.; Nogués, J. Applications of Exchange Coupled Bi-Magnetic Hard/soft and Soft/hard Magnetic Core/shell Nanoparticles. *Phys. Rep.* **2015**, *553*, 1–32.

(4)   Schick, I.; Lorenz, S.; Gehrig, D.; Tenzer, S.; Storck, W.; Fischer, K.; Strand, D.; Laquai, F. F.; Tremel, W. Inorganic Janus Particles for Biomedical Applications. *Beilstein J. Nanotechnol.* **2014**, *5*, 2346–2362.

(5)   Donegá, C. de M. Synthesis and Properties of Colloidal Heteronanocrystals. *Chem. Soc. Rev.* **2011**, *40* (3), 1512–1546.

(6)   Costi, R.; Saunders, A. E.; Banin, U. Colloidal Hybrid Nanostructures: A New Type of Functional Materials. *Angew. Chemie Int. Ed.* **2010**, *49* (29), 4878–4897.

(7)   Yin, H.; Wang, C.; Zhu, H.; Overbury, S. H.; Sun, S.; Dai, S. Colloidal Deposition Synthesis of Supported Gold Nanocatalysts Based on Au–Fe3O4 Dumbbell Nanoparticles. *Chem. Commun.* **2008**, No. 36, 4357–4359.

(8)   Lee, Y.; Garcia, M. A.; Frey Huls, N. A.; Sun, S. Synthetic Tuning of the Catalytic Properties of Au-Fe$_3$O$_4$ Nanoparticles. *Angew. Chemie Int. Ed.* **2010**, *49* (7), 1271–1274.

(9)   Leung, K. C.-F.; Xuan, S.; Zhu, X.; Wang, D.; Chak, C.-P.; Lee, S.-F.; Ho, W. K.-W.; Chung, B. C.-T. Gold and Iron Oxide Hybrid Nanocomposite Materials. *Chem. Soc. Rev.* **2012**, *41* (5), 1911–1928.

(10)   Najafishirtari, S.; Guardia, P.; Scarpellini, A.; Prato, M.; Marras, S.; Manna, L.; Colombo, M. The Effect of Au Domain Size on the CO Oxidation Catalytic Activity of Colloidal Au–FeO$_x$ Dumbbell-like Heterodimers. *J. Catal.* **2016**, *338*, 115–123.

(11)   Wang, C.; Yin, H.; Dai, S.; Sun, S. A General Approach to Noble Metal-Metal Oxide Dumbbell Nanoparticles and Their Catalytic Application for CO Oxidation. *Chem. Mater.* **2010**, *22* (10), 3277–3282.

(12)   Korobchevskaya, K.; George, C.; Diaspro, A.; Manna, L.; Cingolani, R.; Comin, A. Ultrafast Carrier Dynamics in Gold/iron-Oxide Nanocrystal Heterodimers. *Appl. Phys. Lett.* **2011**, *99* (1), 11907.

(13)   Comin, A.; Korobchevskaya, K.; George, C.; Diaspro, A.; Manna, L. Plasmon Bleaching Dynamics in Colloidal Gold–Iron Oxide Nanocrystal Heterodimers. *Nano Lett.* **2012**, *12* (2), 921–926.

(14)   Liu, S.; Guo, S.; Sun, S.; You, X.-Z. Dumbbell-like Au-Fe$_3$O$_4$ Nanoparticles: A New Nanostructure for Supercapacitors. *Nanoscale* **2015**, *7* (11), 4890–4893.

(15)   Zhang, Y.; Zhao, Y.; Yang, Y.; Shen, J.; Yang, H.; Zhou, Z.; Yang, S. A Bifunctional Sensor Based on Au-Fe$_3$O$_4$ Nanoparticle for the Detection of Cd^{2+}. *Sensors Actuators B Chem.* **2015**, *220*, 622–626.

(16) Yu, H.; Chen, M.; Rice, P. M.; Wang, S. X.; White, R. L.; Sun, S. Dumbbell-like Bifunctional Au−Fe$_3$O$_4$ Nanoparticles. *Nano Lett.* **2005**, *5* (2), 379–382.

(17) Wei, Y.; Klajn, R.; Pinchuk, A. O.; Grzybowski, B. A. Synthesis, Shape Control, and Optical Properties of Hybrid Au/Fe$_3$O$_4$ "Nanoflowers." *Small* **2008**, *4* (10), 1635–1639.

(18) Shi, W.; Zeng, H.; Sahoo, Y.; Ohulchanskyy, T. Y.; Ding, Y.; Wang, Z. L.; Swihart, M.; Prasad, P. N. A General Approach to Binary and Ternary Hybrid Nanocrystals. *Nano Lett.* **2006**, *6* (4), 875–881.

(19) Choi, S.-H.; Na, H. Bin; Park, Y. Il; An, K.; Kwon, S. G.; Jang, Y.; Park, M.; Moon, J.; Son, J. S.; Song, I. C.; Moon, W. K.; Hyeon, T. Simple and Generalized Synthesis of Oxide−Metal Heterostructured Nanoparticles and Their Applications in Multimodal Biomedical Probes. *J. Am. Chem. Soc.* **2008**, *130* (46), 15573–15580.

(20) Lin, F.; Doong, R. Characterization of Interfacially Electronic Structures of Gold–magnetite Heterostructures Using X-Ray Absorption Spectroscopy. *J. Colloid Interface Sci.* **2014**, *417*, 325–332.

(21) Schick, I.; Gehrig, D.; Montigny, M.; Balke, B.; Panthöfer, M.; Henkel, A.; Laquai, F.; Tremel, W. Effect of Charge Transfer in Magnetic-Plasmonic Au@MO$_x$ (M = Mn, Fe) Heterodimers on the Kinetics of Nanocrystal Formation. *Chem. Mater.* **2015**, *27* (13), 4877–4884.

(22) Hyeon, T. Chemical Synthesis of Magnetic Nanoparticles. *Chem. Commun.* **2003**, No. 8, 927–934.

(23) Teng, X.; Yang, H. Effects of Surfactants and Synthetic Conditions on the Sizes and Self-Assembly of Monodisperse Iron Oxide Nanoparticles. *J. Mater. Chem.* **2004**, *14* (4), 774–779.

(24) Pichon, B. P.; Gerber, O.; Lefevre, C.; Florea, I.; Fleutot, S.; Baaziz, W.; Pauly, M.; Ohlmann, M.; Ulhaq, C.; Ersen, O.; Pierron-Bohnes, V.; Panissod, P.; Drillon, M.; Begin-Colin, S. Microstructural and Magnetic Investigations of Wüstite-Spinel Core-Shell Cubic-Shaped Nanoparticles. *Chem. Mater.* **2011**, *23* (11), 2886–2900.

(25) Shavel, A.; Rodríguez-González, B.; Spasova, M.; Farle, M.; Liz-Marzán, L. M. Synthesis and Characterization of Iron/iron Oxide Core/shell Nanocubes. *Adv. Funct. Mater.* **2007**, *17* (18), 3870–3876.

(26) Corrias, A.; Mountjoy, G.; Loche, D.; Puntes, V.; Falqui, A.; Zanella, M.; Parak, W. J.; Casula, M. F. Identifying Spinel Phases in Nearly Monodisperse Iron Oxide Colloidal Nanocrystal. *J. Phys. Chem. C* **2009**, *113* (43), 18667–18675.

(27) Pineider, F.; De Julián Fernández, C.; Videtta, V.; Carlino, E.; Al Hourani, A.; Wilhelm, F.; Rogalev, A.; Cozzoli, P. D.; Ghigna, P.; Sangregorio, C. Spin-Polarization Transfer in Colloidal Magnetic-Plasmonic Au/iron Oxide Hetero-Nanocrystals. *ACS Nano* **2013**, *7* (1), 857–866.

(28) Park, J.; An, K.; Hwang, Y.; Park, J.-G.; Noh, H.-J.; Kim, J.-Y.; Park, J.-H.; Hwang, N.-M.; Hyeon, T. Ultra-Large-Scale Syntheses of Monodisperse Nanocrystals. *Nat. Mater.* **2004**, *3* (12), 891–895.

(29) Chidichimo, G.; Cupelli, D.; De Filpo, G.; Formoso, P.; Fiore Pasquale, N. Nanoparticles as a Smart Technology for Remediation. In *Sustainable Development in Chemical*

Engineering; Piemonte, V., De Falco, M., Basile, A., Eds.; John Wiley & Sons, Ltd, 2013; pp 299–348.

(30)   Anastas, P. T.; Alvise, P.; Selva, M. *Handbook of Green Chemistry, Green Processes, Green Nanoscience*; John Wiley & Sons, Ltd: Chichester, UK, 2014.

(31)   Umut, E.; Pineider, F.; Arosio, P.; Sangregorio, C.; Corti, M.; Tabak, F.; Lascialfari, A.; Ghigna, P. Magnetic, Optical and Relaxometric Properties of Organically Coated Gold–magnetite ($Au–Fe_3O_4$) Hybrid Nanoparticles for Potential Use in Biomedical Applications. *J. Magn. Magn. Mater.* **2012**, *324* (15), 2373–2379.

(32)   Rasband, W. . Image J. U. S. National Institutes of Health: Bethesda, Maryland, USA.

(33)   Lutterotti, L.; Matthies, S.; Wenk, H.-R. MAUD: A Friendly Java Program for Material Analysis Using Diffraction. *IUCr Newsl. CPD* **1999**, *21*, 14–15.

(34)   Wu, L.; Mendoza-Garcia, A.; Li, Q.; Sun, S. Organic Phase Syntheses of Magnetic Nanoparticles and Their Applications. *Chem. Rev.* **2016**, *116* (18), 10473–10512.

(35)   Thanh, N. T. K.; Maclean, N.; Mahiddine, S. Mechanisms of Nucleation and Growth of Nanoparticles in Solution. *Chem. Rev.* **2014**, *114* (15), 7610–7630.

(36)   Hyeon, T.; Lee, S. S.; Park, J.; Chung, Y.; Na, H. B. Synthesis of Highly Crystalline and Monodisperse Maghemite Nanocrystallites without a Size-Selection Process. *J. Am. Chem. Soc.* **2001**, *123* (51), 12798–12801.

(37)   Sun, S.; Zeng, H. Size-Controlled Synthesis of Magnetite Nanoparticles. **2002**, No. 31, 8204–8205.

(38)   Jiang, G.; Huang, Y.; Zhang, S.; Zhu, H.; Wu, Z.; Sun, S. Controlled Synthesis of Au–Fe Heterodimer Nanoparticles and Their Conversion into Au–Fe 3 O 4 Heterostructured Nanoparticles. *Nanoscale* **2016**, *8* (41), 17947–17952.

(39)   Casula, M. F.; Jun, Y.; Zaziski, D. J.; Chan, E. M.; Corrias, A.; Alivisatos, A. P. The Concept of Delayed Nucleation in Nanocrystal Growth Demonstrated for the Case of Iron Oxide Nanodisks. *J. Am. Chem. Soc.* **2006**, *128* (5), 1675–1682.

(40)   Moya, C.; Batlle, X.; Labarta, A. The Effect of Oleic Acid on the Synthesis of $Fe_{3-x}O_4$ Nanoparticles over a Wide Size Range. *Phys. Chem. Chem. Phys.* **2015**, *17* (41), 27373–27379.

(41)   Sun, S.; Zeng, H.; Robinson, D. B.; Raoux, S.; Rice, P. M.; Wang, S. X.; Li, G. Monodisperse MFe_2O_4 (M = Fe, Co, Mn) Nanoparticles. *J. Am. Chem. Soc.* **2004**, *126* (1), 273–279.

(42)   Shemer, G.; Tirosh, E.; Livneh, T.; Markovich, G. Tuning a Colloidal Synthesis to Control Co^{2+} Doping in Ferrite Nanocrystals. *J. Phys. Chem. C* **2007**, *111* (39), 14334–14338.

(43)   Roca, A. G.; Niznansky, D.; Poltierova-Vejpravova, J.; Bittova, B.; González-Fernández, M. A.; Serna, C. J.; Morales, M. P. Magnetite Nanoparticles with No Surface Spin Canting. *J. Appl. Phys.* **2009**, *105* (11), 114309.

(44)   Buck, M. R.; Schaak, R. E. Emerging Strategies for the Total Synthesis of Inorganic Nanostructures. *Angew. Chem. Int. Ed.* **2013**, *52* (24), 6154–6178.

(45)   Hiramatsu, H.; Osterloh, F. E. A Simple Large-Scale Synthesis of Nearly Monodisperse

Gold and Silver Nanoparticles with Adjustable Sizes and with Exchangeable Surfactants. *Chem. Mater.* **2004**, *16* (13), 2509–2511.

(46) Peng, S.; Lee, Y.; Wang, C.; Yin, H.; Dai, S.; Sun, S. A Facile Synthesis of Monodisperse Au Nanoparticles and Their Catalysis of CO Oxidation. *Nano Res.* **2008**, *1* (3), 229–234.

(47) Bastús, N. G.; Comenge, J.; Puntes, V. Kinetically Controlled Seeded Growth Synthesis of Citrate-Stabilized Gold Nanoparticles of up to 200 Nm: Size Focusing versus Ostwald Ripening. *Langmuir* **2011**, *27* (17), 11098–11105.

(48) Lee, J.; Zhang, S.; Sun, S. High-Temperature Solution-Phase Syntheses of Metal-Oxide Nanocrystals. *Chem. Mater.* **2013**, *25* (8), 1293–1304.

(49) Yedra, L.; Xuriguera, E.; Estrader, M.; López-Ortega, A.; Baró, M. D.; Nogués, J.; Roldan, M.; Varela, M.; Estradé, S.; Peiró, F. Oxide Wizard: An EELS Application to Characterize the White Lines of Transition Metal Edges. *Microsc. Microanal.* **2014**, *20* (3), 698–705.

(50) Ewels, P.; Sikora, T.; Serin, V.; Ewels, C. P.; Lajaunie, L. A Complete Overhaul of the Electron Energy-Loss Spectroscopy and X-Ray Absorption Spectroscopy Database: Eelsdb.eu. *Microsc. Microanal.* **2016**, *22* (3), 717–724.

(51) Caruntu, D.; Caruntu, G.; O'Connor, C. J. Magnetic Properties of Variable-Sized Fe_3O_4 Nanoparticles Synthesized from Non-Aqueous Homogeneous Solutions of Polyols. *J. Phys. D. Appl. Phys.* **2007**, *40* (19), 5801–5809.

(52) Sarveena, S.; Muraca, D.; Zélis, P. M.; Javed, Y.; Ahmad, N.; Vargas, J. M.; Moscoso-Londoño, O.; Knobel, M.; Singh, M.; Sharma, S. K. Surface and Interface Interplay on the Oxidizing Temperature of Iron Oxide and Au–iron Oxide Core–shell Nanoparticles. *RSC Adv.* **2016**, *6* (74), 70394–70404.

(53) Salazar-Alvarez, G.; Qin, J.; Šepelák, V.; Bergmann, I.; Vasilakaki, M.; Trohidou, K. N.; Ardisson, J. D.; Macedo, W. A. A.; Mikhaylova, M.; Muhammed, M.; Baró, M. D.; Nogués, J. Cubic versus Spherical Magnetic Nanoparticles: The Role of Surface Anisotropy. *J. Am. Chem. Soc.* **2008**, *130* (40), 13234–13239.

(54) Lopes, G.; Vargas, M.; Sharma, S. K.; Be, F.; Pirota, K. R.; Knobel, M.; Rettori, C.; Zysler, R. D. Ag-Fe_3O_4 Dimer Colloidal Nanoparticles : Synthesis and Enhancement of Magnetic Properties. *J. Phys. Chem. C* **2010**, *114* (22), 10148–10152.

(55) Estrader, M.; López-Ortega, A.; Golosovsky, I. V; Estradé, S.; Roca, A. G.; Salazar-Alvarez, G.; López-Conesa, L.; Tobia, D.; Winkler, E.; Ardisson, J. D.; Macedo, W. A. A.; Morphis, A.; Vasilakaki, M.; Trohidou, K. N.; Gukasov, A.; Mirebeau, I.; Makarova, O. L.; Zysler, R. D.; Peiró, F.; Baró, M. D.; Bergström, L.; Nogués, J. Origin of the Large Dispersion of Magnetic Properties in Nanostructured Oxides: Fe_xO/Fe_3O_4 Nanoparticles as a Case Study. *Nanoscale* **2015**, *7* (7), 3002–3015.

(56) Feygenson, M.; Bauer, J. C.; Gai, Z.; Marques, C.; Aronson, M. C.; Teng, X.; Su, D.; Stanic, V.; Urban, V. S.; Beyer, K. A.; Dai, S. Exchange Bias Effect in Au-Fe_3O_4 Dumbbell Nanoparticles Induced by the Charge Transfer from Gold. *Phys. Rev. B* **2015**, *92* (5), 54416.

(57) Zeng, H.; Sun, S. Syntheses, Properties, and Potential Applications of Multicomponent Magnetic Nanoparticles. *Adv. Funct. Mater.* **2008**, *18* (1), 391–400.

(58) Sepúlveda, B.; Angelomé, P. C.; Lechuga, L. M.; Liz-Marzán, L. M. LSPR-Based Nanobiosensors. *Nano Today* **2009**, *4* (3), 244–251.

(59) González-Díaz, J. B.; García-Martín, A.; García-Martín, J. M.; Cebollada, A.; Armelies, G.; Sepúlveda, B.; Alaverdyan, Y.; Käll, M. Plasmonic Au/Co/Au Nanosandwiches with Enhanced Magneto-Optical Activity. *Small* **2008**, *4* (2), 202–205.

(60) Yi, D. K.; Selvan, S. T.; Lee, S. S.; Papaefthymiou, G. C.; Kundaliya, D.; Ying, J. Y. Silica-Coated Nanocomposites of Magnetic Nanoparticles and Quantum Dots. *J. Am. Chem. Soc.* **2005**, *127* (14), 4990–4991.

(61) Han, Y.; Jiang, J.; Lee, S. S.; Ying, J. Y. Reverse Microemulsion-Mediated Synthesis of Silica-Coated Gold and Silver Nanoparticles. *Langmuir* **2008**, *24* (11), 5842–5848.

Table of Contents